THE ASTRONOMICAL JOURNAL, 165:218 (10pp), 2023 May https://doi.org/10.3847/1538-3881/acc651

TOI-5375 B: A Very Low Mass Star at the Hydrogen-burning Limit Orbiting an Early M-type Star*†

Mika Lambert[1], Chad F. Bender[1], Shubham Kanodia[2], Caleb I. Cañas[3,4,5], Andrew Monson[1], Gudmundur Stefánsson[6,16], William D. Cochran[7,8], Mark E. Everett[9], Arvind F. Gupta[4,5], Fred Hearty[10], Henry A. Kobulnicky[10], Jessica E. Libby-Roberts[4,5], Andrea S. J. Lin[4,5,5], Suvrath Mahadevan[4,5,11], Joe P. Ninan[12], Brock A. Parker[10], Paul Robertson[13], Christian Schwab[14], and Ryan C. Terrien[15]

[1] Steward Observatory and Department of Astronomy, University of Arizona, 933 N. Cherry Avenue, Tucson, AZ 85721, USA; mlambert43@arizona.edu
[2] Earth and Planets Laboratory, Carnegie Institution for Science, 5241 Broad Branch Road, NW, Washington, DC 20015, USA
[3] NASA Goddard Space Flight Center, 8800 Greenbelt Road, Greenbelt, MD 20771, USA
[4] Department of Astronomy & Astrophysics, 525 Davey Laboratory, The Pennsylvania State University, University Park, PA 16802, USA
[5] Center for Exoplanets and Habitable Worlds, 525 Davey Laboratory, The Pennsylvania State University, University Park, PA 16802, USA
[6] Department of Astrophysical Sciences, Princeton University, 4 Ivy Lane, Princeton, NJ 08540, USA
[7] McDonald Observatory and Department of Astronomy, The University of Texas at Austin, Austin, TX, USA
[8] Center for Planetary Systems Habitability, The University of Texas at Austin, Austin, TX, USA
[9] NSF's National Optical-Infrared Astronomy Research Laboratory, 950 N. Cherry Avenue, Tucson, AZ 85719, USA
[10] Department of Physics & Astronomy, University of Wyoming, Laramie, WY 82070, USA
[11] ETH Zurich, Institute for Particle Physics & Astrophysics, Zurich, Switzerland
[12] Department of Astronomy and Astrophysics, Tata Institute of Fundamental Research, Homi Bhabha Road, Colaba, Mumbai 400005, India
[13] Department of Physics & Astronomy, University of California Irvine, Irvine, CA 92697, USA
[14] School of Mathematical and Physical Sciences, Macquarie University, Balaclava Road, North Ryde, NSW 2109, Australia
[15] Carleton College, One North College Street, Northfield, MN 55057, USA
Received 2022 December 15; revised 2023 March 19; accepted 2023 March 20; published 2023 April 28

Abstract

The Transiting Exoplanet Survey Satellite (TESS) mission detected a companion orbiting TIC 71268730, categorized it as a planet candidate, and designated the system TOI-5375. Our follow-up analysis using radial-velocity data from the Habitable-zone Planet Finder, photometric data from Red Buttes Observatory, and speckle imaging with NN-EXPLORE Exoplanet Stellar Speckle Imager determined that the companion is a very low mass star near the hydrogen-burning mass limit with a mass of $0.080 \pm 0.002 M_{\odot}$ ($83.81 \pm 2.10 M_J$), a radius of $0.1114^{+0.0048}_{-0.0050} R_{\odot}$ ($1.0841^{0.0467}_{0.0487} R_J$), and brightness temperature of 2600 ± 70 K. This object orbits with a period of 1.721553 ± 0.000001 days around an early M dwarf star ($0.62 \pm 0.016 M_{\odot}$). TESS photometry shows regular variations in the host star's TESS light curve, which we interpreted as an activity-induced variation of ∼2%, and used this variability to measure the host star's stellar rotation period of $1.9716^{+0.0080}_{-0.0083}$ days. The TOI-5375 system provides tight constraints on stellar models of low-mass stars at the hydrogen-burning limit and adds to the population in this important region.

Unified Astronomy Thesaurus concepts: Binary stars (154); Low mass stars (2050)

1. Introduction

The Transiting Exoplanet Survey Satellite (TESS; Ricker et al. 2015) is a NASA mission to monitor nearly the entire sky for brief decreases in brightness caused by transiting planetary objects. However, a significant number of these transits are astrophysical false positives, caused by stellar binary systems. Since the launch of TESS in 2018, there have been 234 confirmed planets and 1573 false positives detected (Guerrero et al. 2021). Ground-based follow-up is essential to fully characterize these objects.

Eclipsing binary systems are important astrophysical benchmarks because they allow us to dynamically constrain the physical characteristics of the system including mass and radius (e.g., Torres et al. 2009; Kesseli et al. 2019; Serenelli et al. 2021) mostly independent of theoretical models. Thus, these stellar systems provide measurements that feedback into the calibration and evolution of stellar evolution models. Cataloging false positives in TESS data may also benefit the TESS data-processing pipeline to identify parameters that are correlated with erroneously classifying binary systems as exoplanets.

The TESS input catalog identified TIC 71268730 (TOI-5375, 2MASS J07350822+7124020, Gaia DR3 1110586978339817728) as an early M dwarf with an effective temperature of 3865 ± 157 K. The TESS data-processing pipeline designated the companion of TOI-5375 as a candidate planet with a period of 1.72 days and a depth of 36.88 ± 0.58 mmag. Gan et al. (2023) classified TOI-5375 as a verified planet candidate after vetting by their photometric analysis pipeline. In this paper, we present our analysis of the TOI-5375 system augmenting the TESS photometry with ground-based observations to determine the

* Based on observations obtained with the Hobby–Eberly Telescope (HET), which is a joint project of the University of Texas at Austin, the Pennsylvania State University, Ludwig-Maximillians-Universitaet Muenchen, and Georg-August Universitaet Goettingen. The HET is named in honor of its principal benefactors, William P. Hobby and Robert E. Eberly.

† The WIYN Observatory is a joint facility of the NSF's National Optical-Infrared Astronomy Research Laboratory, Indiana University, the University of Wisconsin-Madison, Pennsylvania State University, the University of Missouri, the University of California-Irvine, and Purdue University.

[16] NASA Sagan Fellow.

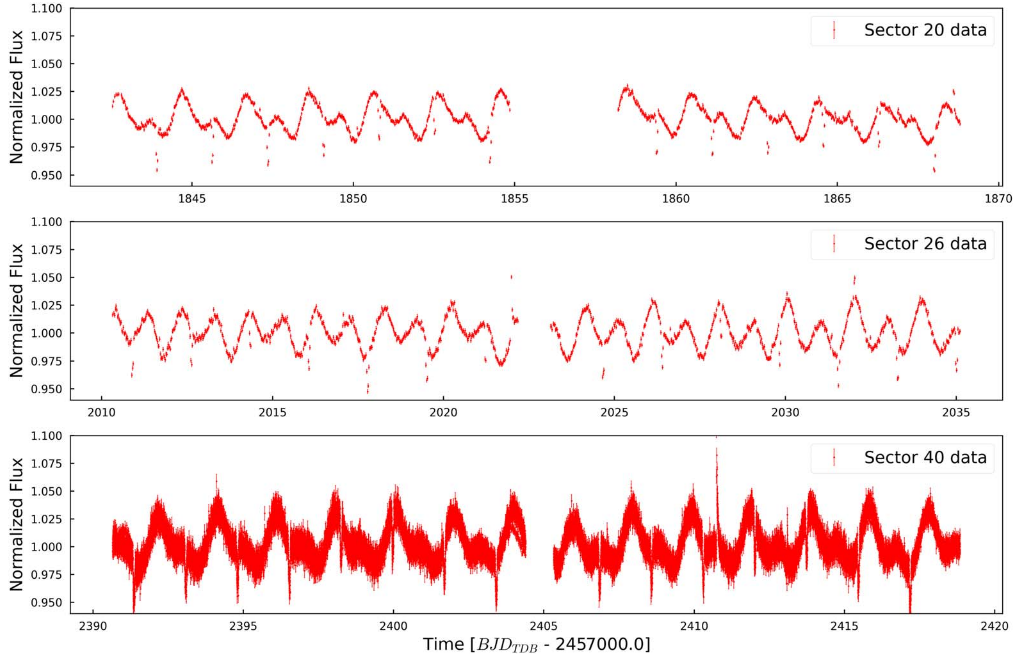

Figure 1. Long-cadence (1800 s), unbinned transit observations of TOI-5375 in TESS Sectors 20 (top) and 26 (middle), and short-cadence (120 s) unbinned photometry from TESS Sector 40 (bottom). Variability in the host star's light curve evolves throughout the different sectors, which we infer to be due to varying stellar spots. The periodicity of the spot-induced variability is tied to the rotation of the primary star. We also see flares due to stellar activity, which are masked out in our analysis.

companion, TOI-5375 B, is a very low mass star (VLMS) at the hydrogen-burning mass limit. In Section 2, we describe the observational data collected; in Section 3, we discuss the stellar parameters; in Section 4, we discuss the resulting posteriors of our joint fit; in Section 5 we present an analysis of our results in the context of evolutionary models, age, temperature, and environment.

2. Observations

2.1. TESS Photometry

TOI-5375 was observed by TESS in Sector 20 from 2019 December 24–2020 January 21, and in Sector 26 from 2020 June 8–2020 July 4, at a 30 minute (1800 s) cadence. It was also observed in Sector 40 from 2021 June 24–2021 July 23, at 120 s cadence. Similar to the TOI-1899 (Cañas et al. 2020) and TOI-3629 (Cañas et al. 2022) systems, we identified TOI-5375 B as a planetary candidate using a custom pipeline to search for transiting candidates in short- and long-cadence TESS data orbiting M dwarfs that were amenable to radial-velocity (RV) observations with the Habitable-zone Planet Finder (HPF; see Cañas et al. 2022). TOI-5375 B was also independently identified by the TESS science-processing pipeline (Jenkins et al. 2016) with a period of about 1.72 days and a transit duration of 1.74 hr. For the short-cadence data, Sector 40, we obtained the Pre-search Data Conditioning SAP (PSDCSAP) flux data from the Mikulski Archive for Space Telescopes (MAST).

We used `eleanor` (Feinstein et al. 2019) to produce the light curves from the TESS full-frame images of Sectors 20 and 26. `eleanor` uses the TESScut[17] service to obtain a cutout of 31×31 pixels from the calibrated full-frame images centered on the target. In order to derive the light curve, we used the `CORRFLUX` values, in which `eleanor` uses linear regression with pixel position, measured background, and time to remove signals correlated with these parameters. We set the aperture mode to "normal," which tests different apertures and is based on the magnitude of the target star and the contamination ratio from TESS (Feinstein et al. 2019). Figure 1 shows the original light curves of TOI-5375 in TESS Sectors 20, 26, and 40. Several strong flares are clearly seen in the light curves. We identified and masked these events by hand before carrying out subsequent analysis.

2.2. Ground-based Follow-up

2.2.1. RBO Photometry

We observed TOI-5375 on the night of 2022 April 4 UT using the 0.6 m telescope at Red Buttes Observatory (RBO) in Wyoming (Kasper et al. 2016). RBO is equipped with an Andor Apogee Alta F16 camera and uses the 2×2 on-chip binning mode, which has a gain of 1.4 e^-/ADU and a plate scale of $0\farcs73$ pixel^{-1}. All observations were obtained in the Bessell *I* filter (Bessell 1990). The target was defocused moderately and observed using an exposure time of 240 s. Observations ranged from an airmass of 1.18 to 2.15. We processed the RBO light curves using AstroImageJ (Collins et al. 2017). The final reductions used a photometric aperture radius of 12 pixels ($8\farcs76$), an inner sky radius of 18 pixels ($13\farcs14$), and an outer sky radius of 25 pixels ($18\farcs25$).

2.2.2. HPF Radial Velocities

From 2020 November to 2022 January, we used the HPF (Mahadevan et al. 2014) to obtain 12 exposures of TOI-5375. HPF is a high-resolution, near-infrared (8080–12780 Å) Doppler spectrograph at the 10 m Hobby–Eberly Telescope (HET) located in Texas (Ramsey et al. 1998; Bash 2001). We

[17] https://mast.stsci.edu/tesscut/

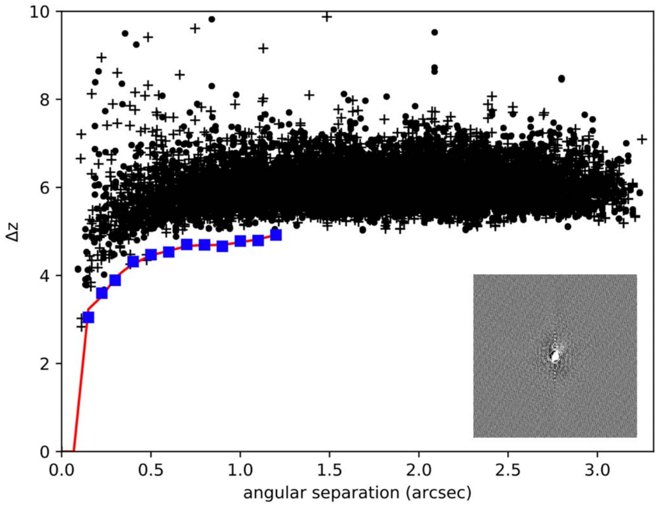

Figure 2. Speckle contrast curve of TOI-5375 from the Sloan z' filter using NESSI. The blue squares are 5σ contrast limits at each angular separation with a spline fit in red. The black plus signs are the extreme local maxima and the black dots are extreme local minima for the sensitivity limits. The data reveals no bright companions and no significant sources of dilution at separations from 0.″2 to 1.″2 from TOI-5375. The inset is the 4.″7 × 4.″7 NESSI speckle image centered on TOI-5375 in the z' filter.

Table 1
HPF Observations of TOI-5375

BJD[a]	RV (m s^{-1})	σ (m s^{-1})	S/N[b]
2,459,159.972591	1077.82	95.49	57
2,459,159.984070	1458.72	101.72	55
2,459,159.995844	2260.30	93.86	60
2,459,268.667101	9694.40	140.97	42
2,459,268.675136	9903.73	161.72	37
2,459,268.683141	9943.74	117.58	50
2,459,517.999874	−2325.99	115.32	50
2,459,520.006804	9021.04	109.39	52
2,459,530.957075	−17331.27	82.48	66
2,459,538.950183	10048.02	124.83	48
2,459,547.928928	−1769.31	92.52	60
2,459,596.774456	−25396.43	87.53	63

Notes.
[a] BJD is the Barycentric Julian Date.
[b] The signal-to-noise ratio (S/N) is the sn18 value, which is the median S/N of order 18 at 1070 nm. The exposure times are 945 s, except for 2,459,268.667101, 2,459,268.675136, and 2,459,268.683141, which are 630 s.

used the tool HxRGproc to convert the raw HPF data into flux images and correct nonlinearity and cosmic rays, remove bias noise, and calculate the slope/flux and variance image (Ninan et al. 2018).

We analyzed the HPF spectra to measure the RVs using the method in Stefansson et al. (2020), which uses a modified version of the SpEctrum Radial Velocity AnaLyser pipeline (SERVAL; Zechmeister et al. 2018) that has been optimized for HPF data. HPF-adapted SERVAL first creates a master template from the target star observations and then moves it in velocity space to determine the Doppler shift for each observation. SERVAL then compares the observation with the template and minimizes the χ^2 statistic. The telluric regions are identified by a synthetic telluric-line mask created by telfit (Gullikson et al. 2014), a Python wrapper to the Line-by-Line Radiative Transfer Model package (Clough et al. 2005).

Table 2
Priors Used in the Joint Fit

Parameter	Description	Model[a]
Orbital Parameters:		
P	Orbital period (days)	$\mathcal{N}$(1.72154439, 0.1)
T_0	Transit midpoint (BJD$_{\rm TDB}$)	$\mathcal{N}$(2459391.4, 0.1)
$\log(R_B/R_A)$	Scaled radius	$\mathcal{L}$(−1.66211817, 1)
log(K)	RV semiamplitude (m s^{-1})	$\mathcal{U}$(0, 10)
b	Impact parameter	$\mathcal{U}$(0, 1)
Other Constraints:		
R_A	Stellar radius ($R_\odot$)	$\mathcal{N}$(0.649, 0.024)
M_A	Mass of star ($M_\odot$)	$\mathcal{N}$(0.62, 0.016)
M_B	Mass of companion ($M_\oplus$)	$\mathcal{U}$(0.1, 3 ∗ 10^6)
q	Mass ratio	$\mathcal{U}$(0, 1)
S	Surface brightness ratio	$\mathcal{U}$(0, 1)
$T_{{\rm eff}A}$	Effective temperature of the host star (K)	$\mathcal{N}$(3897, 88)
Jitter and Instrumental Terms:		
γ	Gamma velocity (m s^{-1})	$\mathcal{N}$(1859, 20000)
u_1	Limb-darkening parameter[b]	$\mathcal{U}$(0, 1)
u_2	Limb-darkening parameter[b]	$\mathcal{U}$(0, 1)
dv/dt	HPF RV trend (mm s^{-1} yr^{-1})	$\mathcal{N}$(0, 5)
sigma$_{\rm RV}$	RV jitter (m s^{-1})	$\mathcal{N}$(10^{-3}, 10^3)
$D_{\rm TESS}$	TESS dilution	$\mathcal{U}$(0.1, 1.5)
Q	Quality factor for secondary oscillation	$\mathcal{U}$(0.01, 500.0)
dQ	Difference between quality factor for primary and secondary model	$\mathcal{U}$(0.01, 500.0)
f	Fractional amplitude of secondary	$\mathcal{U}$(0.01, 1.0)
$\log(\sigma_{\rm phot})$	Log jitter	$\mathcal{U}$(−6, 1)

Notes.
[a] $\mathcal{N}$ is normal, $\mathcal{U}$ is uniform, $\mathcal{L}$ is log normal.
[b] Each object in the binary system has an independent limb-darkening parameter associated with it. The limb-darkening parameters are used in the secondary eclipse function.

Table 3
Summary of the Primary Star's Stellar Parameters

Parameter[a]	Description	Model
R_A	Stellar radius ($R_\odot$)	0.649 ± 0.024
M_A	Stellar mass ($M_\odot$)	0.620 ± 0.016
ρ_A	Density (cgs)	$3.83^{+0.28}_{-0.24}$
A_v	V-band extinction (mag)	$0.017^{+0.014}_{-0.012}$
$T_{\rm eff}$ (K)	Effective temperature (K)	3897 ± 88
[Fe/H]	Metallicity (dex)	0.29 ± 0.12
$\log(g)$	Surface gravity (cgs)	4.68 ± 0.046
$v \sin i_A$	Rotational broadening (km s^{-1})	16.7 ± 0.9
d	distance (pc)	121.14 ± 0.20

Note.
[a] Stellar parameters are derived from HPF − SpecMatch.

After masking out the telluric and sky-emission lines, the master template is created using all of the HPF observations for this target. We used barycorrpy (Kanodia & Wright 2018) to account for the barycentric correction on each spectra. The RVs, 1σ RV uncertainty, signal-to-noise ratio, and exposure times are listed in Table 1.

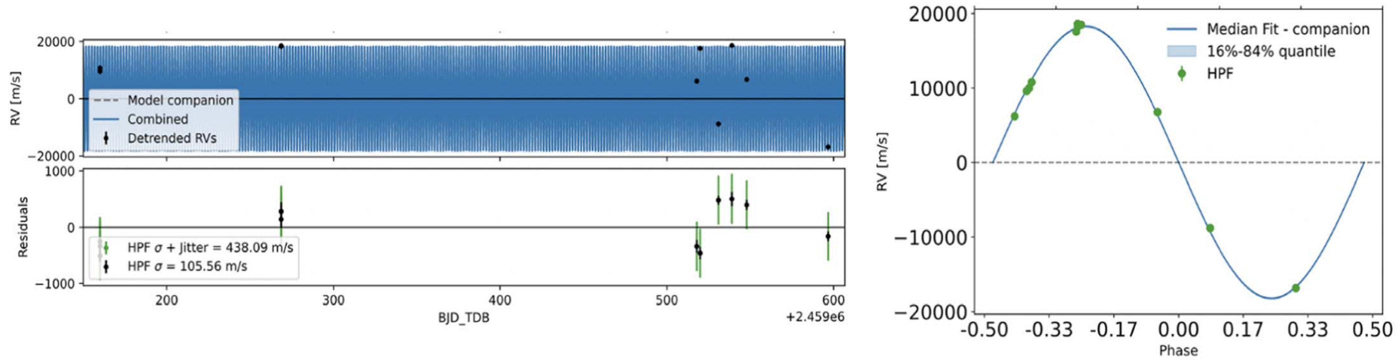

Figure 3. Top left: RV data points in black with the best-fitting joint fit model overlaid in blue. Bottom left: residuals from the best-fit model. Right: phase-folded RVs with the best-fitting joint fit model overlaid.

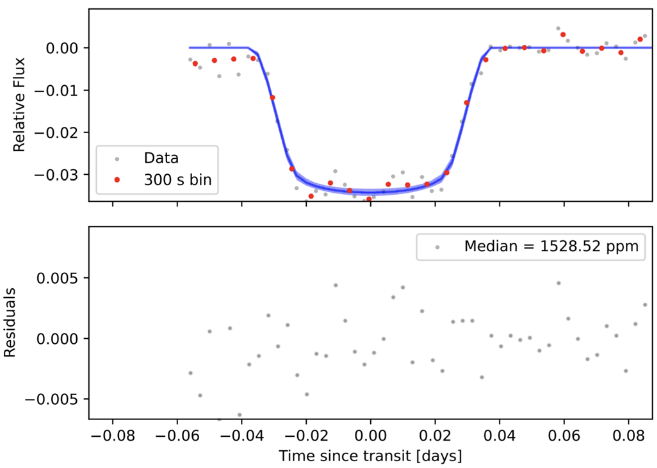

Figure 4. Top: light curve of RBO data of an exposure time of 240 s normalized and detrended using AstroImageJ. The MCMC model is overlaid with the blue shaded region indicating a 1σ deviation. Bottom: residuals of this model with a median value of 1528.52 ppm.

2.3. NESSI Speckle Imaging

To investigate the possibility of bright background sources contaminating our RBO photometry, we observed TOI-5375 with the NN-Explore Exoplanet Stellar Speckle Imager (NESSI; Scott et al. 2018) on the WIYN 3.5 m telescope at Kitt Peak National Observatory on the night of 2022 April 21. A 9 minute sequence of 40 ms diffraction-limited speckle images was taken in the Sloan *z*' filter with NESSI's red camera. A reconstructed speckle image was generated following the procedures described in Howell et al. (2011). Figure 2 shows the contrast curve along with an inset of the NESSI speckle image in the *z*' filter. We conclude that there are no close by sources with magnitudes brighter than $\Delta z' = 4.45$ for separations $> 0\farcs5$.

3. Stellar Parameters

`HPF − SpecMatch` (Stefansson et al. 2020) uses the empirical template matching methodology discussed in Yee et al. (2017) to derive stellar parameters of the host star from HPF spectra. We used this package to calculate the stellar parameters effective temperature ($T_{\rm eff}$), surface gravity (log(g)), metallicity ([Fe/H]), and $v \sin i_A$. `HPF − SpecMatch` identifies the spectra that best match well-characterized stars from a library using χ^2 minimization. Then, it creates a composite spectrum using a weighted, linear combination of the five best-matching library spectra and derives the stellar properties using these weights. While searching for the best-matching library spectra, `HPF − SpecMatch` uses a linear limb-darkening law to broaden the stellar templates. We determined TOI-5375 has a $T_{\rm eff}$ of 3897 ± 88 K, a log(g) of 4.68 ± 0.046, a [Fe/H] of 0.29 ± 0.12, and a $v \sin i_A$ of 16.7 ± 0.9 km s^{-1}. The reported uncertainty is the standard deviation of the residuals from a leave-one-out cross-validation procedure applied to the entire spectral library in the chosen spectral order.

We derived the model-dependent stellar parameters, mass and radius, using the spectral energy distribution (SED) that uses the `EXOFASTv2` analysis package (Eastman et al. 2019). `EXOFASTv2` calculates the bolometric corrections for the SED fit by linearly interpolating the precomputed bolometric corrections[18] of log(g), $T_{\rm eff}$, [Fe/H], and AV from the MIST model grids (Dotter 2016; Choi et al. 2016). The SED fit uses Gaussian priors on (i) 2MASS *J*, *H*, *K* magnitudes; Sloan *g*', *r*', *i*' magnitudes and Johnson *B*, *V* magnitudes from Henden et al. (2018); and Wide-field Infrared Survey Explorer magnitudes (Wright et al. 2010); (ii) log(g), $T_{\rm eff}$, and [Fe/H] derived from `HPF − SpecMatch`; and (iii) the geometric distance calculated from Bailer-Jones et al. (2021).

We applied an upper limit to the visual extinction based on estimates of Galactic dust (Green et al. 2019) calculated at the distance determined by Bailer-Jones et al. (2021). We converted the extinction from Green et al. (2019) to a visual magnitude extinction using the $Rv = 3.1$ reddening law from Fitzpatrick 1999). Table 2 contains the priors used in the joint fit described in Section 4, and Table 3 contains the stellar parameters derived from our HPF SpecMatch analysis with their uncertainties. The model-dependent mass and radius are 0.649 ± 0.024 $M_\odot$ and 0.620 ± 0.016 $R_\odot$, respectively.

4. Data Analysis

4.1. Joint Fitting with Photometry and RV Data

We used the `exoplanet` modeling code (Foreman-Mackey et al. 2021b) to carry out a joint fit of TESS, RBO, and HPF data. `exoplanet` implements a Hamiltonian Monte Carlo (HMC) parameter estimation from PyMC3 (Salvatier et al. 2016) using the Gelman–Rubin statistic of $\hat{R} \leqslant 1.1$ (Ford 2006) to check for convergence.

`exoplanet` uses `starry` (Luger et al. 2019; Agol et al. 2020) to model the transits and uses a separate quadratic limb-darkening term for each instrument. Each sector was fit with an

[18] https://waps.cfa.harvard.edu/MIST/model_grids.html#bolometric

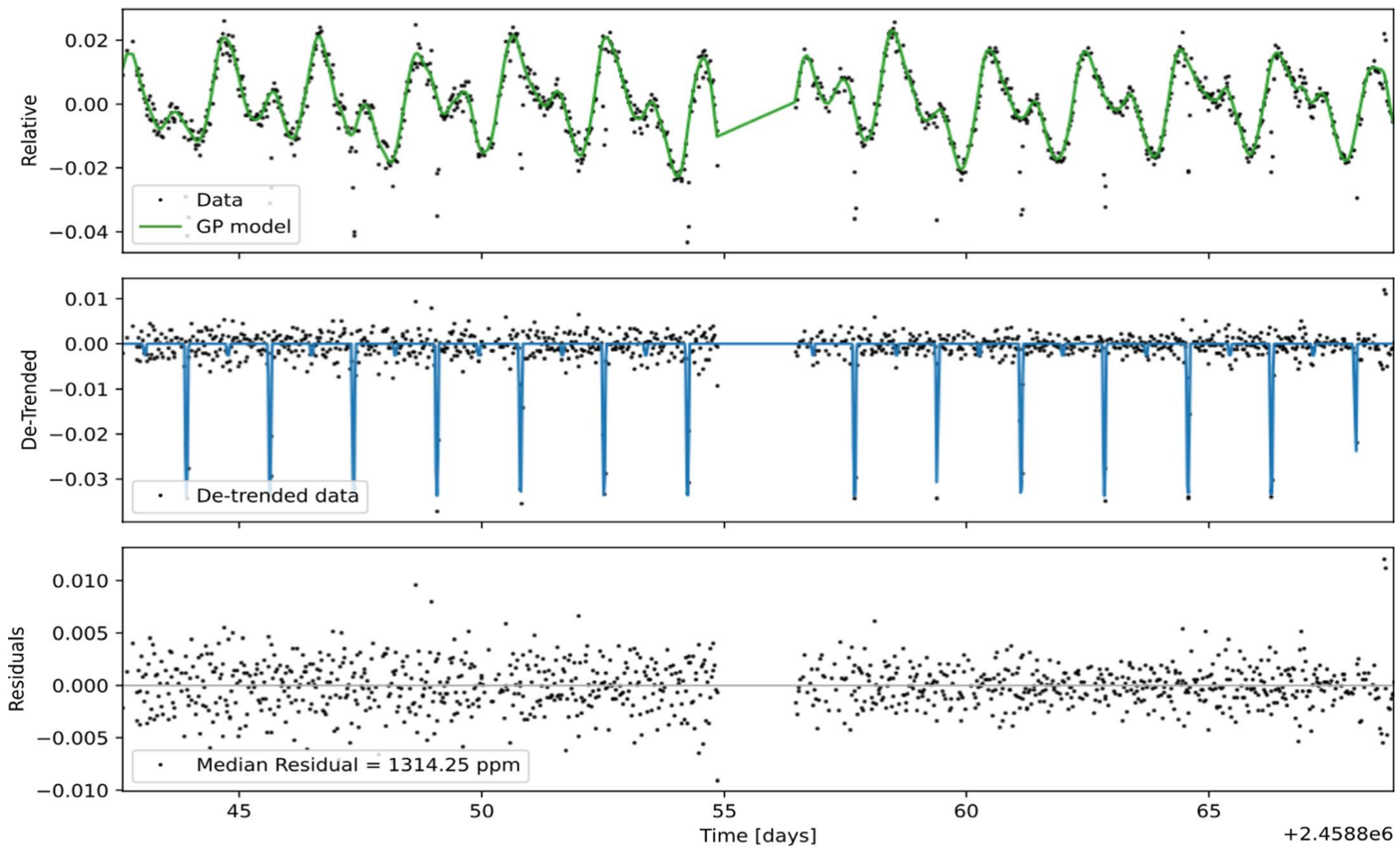

Figure 5. Representative example of TESS Sector 20 photometry along with a stellar rotation GP kernel is shown in the top panel. The detrended photometry is shown in the middle panel, with the eclipses overlaid in blue. The bottom panel shows the residuals.

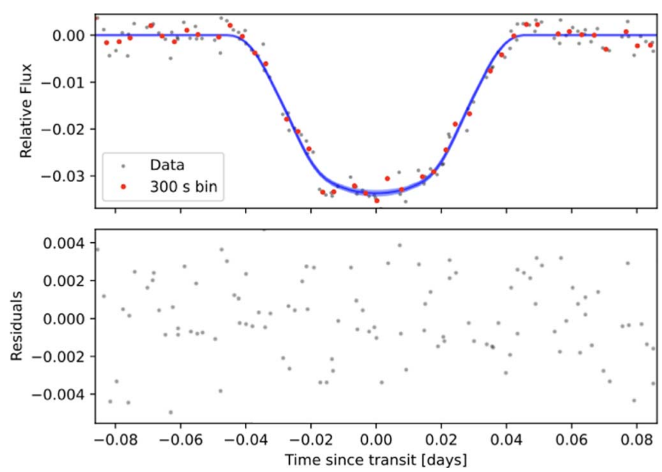

Figure 6. Phase-folded photometric observations for TOI-5375 in Sector 20. The gray points are the detrended data, the red points are 300 s bins, and the model is shown in blue with a thin blue shaded region indicating a 1σ deviation. The median residual value for the joint fit over all sectors and including the primary and secondary eclipse is 1330 ppm.

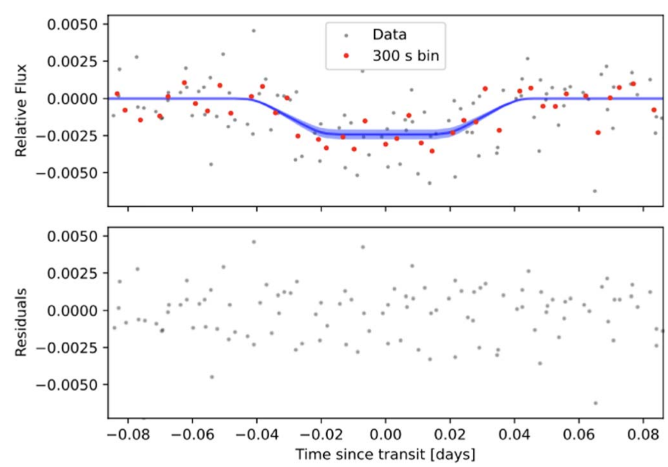

Figure 7. Phase-folded photometric observations of the secondary eclipse for TOI-5375 in Sector 20. Plot markers are identical to those used in Figure 6.

independent limb-darkening coefficient. For uninformative limb-darkening priors, we reparameterized the priors following the procedure described in Kipping (2013). We included a jitter term as a simple noise model for each photometric data set. We assumed a circular orbit and fix the eccentricity to zero. We also used a dilution term on the photometric model because we want to account for potentially blended background stars in the TESS data. We did not include the dilution term for the RBO data because the higher spatial resolution compared to TESS allows for the star to be isolated from background stars, and our NESSI data confirm that there are no background objects within the RBO point-spread function.

We used the standard Keplerian model for the RVs. The photometric model includes the quadratic limb-darkening law (Kipping 2013). We simultaneously fit a Gaussian Process (GP) to the photometric data to detrend the light curve and extracted the transits. Our GP kernel is a mixture of two simple harmonic oscillator terms that can be used to model stellar rotation as a stochastically driven, damped harmonic oscillator (Foreman-Mackey et al. 2017; Foreman-Mackey 2018). We

Table 4
Derived Parameters of TOI-5375 Using the Limb-darkening Joint Fit Model

Parameter	Unit	Value
Parameters:		
Period	P (days)	$1.72155391^{+0.00000144}_{-0.00000142}$
Impact parameter	b	$0.24^{+0.12}_{-0.14}$
Semiamplitude velocity	K_0 (m s^{-1})	$18256.82^{+209.84}_{-208.49}$
RV trend	dv/dt (m s^{-1} yr^{-1})	$0.14^{+4.92}_{-5.07}$
RV jitter	$\sigma_{\rm HPF}$ (m s^{-1})	$424.25^{+134.28}_{-89.55}$
RV offset	$\gamma_{\rm HPF}$ (m s^{-1})	$-8535.87^{+163.89}_{-164.016}$
Transit Parameters:		
Transit midpoint	T_0 (BJD$_{\rm TDB}$)	$2458843.91098 \pm 0.00032$
Scaled radius	R_B/R_A	0.1493 ± 0.0030
Flux ratio	S	$0.086^{+0.012}_{-0.011}$
Scaled semimajor axis	a/R_A	$8.65^{+0.20}_{-0.25}$
Eclipse depth	$F_{\rm ecl}$	$0.00193^{+0.00026}_{-0.00025}$
Inclination	i (deg)	$88.41^{+0.97}_{-0.86}$
Transit duration	T_{14} (days)	$0.07126^{+0.00097}_{-0.00095}$
Photometric jitter	$\sigma_{\rm TESS\ S20}$	$0.001740^{+0.000081}_{-0.000082}$
	$\sigma_{\rm TESS\ S26}$	$0.001626^{+0.00013}_{-0.00012}$
	$\sigma_{\rm TESS\ S40}$	0.001931 ± 0.000093
	$\sigma_{\rm RBO}$ [a]	$0.00195^{+0.00028}_{-0.00027}$
Dilution	$D_{\rm TESS\ S20}$	$0.926^{+0.033}_{-0.032}$
	$D_{\rm TESS\ S26}$	$0.821^{+0.033}_{-0.031}$
	$D_{\rm TESS\ S40}$	$0.710^{+0.024}_{-0.023}$
Rotation period	Prot (days)	$1.9716^{+0.0080}_{-0.0083}$
Companion Parameters:		
Radius	R_B ($R_\oplus$)	$10.71^{+2.057}_{-0.97}$
	R_B (R_J)	$0.96^{+0.18}_{-0.087}$
	R_B ($R_\odot$)	$0.098^{+0.019}_{-0.0089}$
Mass	M_B ($M_\oplus$)	26642.4 ± 666.06
	M_B (M_J)	84.37 ± 2.02
	M_B ($M_\odot$)	0.080 ± 0.002
Temperature	T_B (K)	2600 ± 70
Semimajor axis	a (au)	$0.02484^{+0.00024}_{-0.00026}$

Note.
[a] RBO parameters come from a joint fit using the quadratic limb-darkening function.

used this kernel to model the quasiperiodic signal for our likelihood function for TESS photometry. We also assumed a linear trend for the RV data. Figure 3 shows the best-fit model overlaid on the RV data with the residuals plotted in the bottom left panel and shows the phase-folded RVs along with the best-fit model. We note that the jitter term is relatively high compared to other HPF measurements due to the stellar activity and variability of the star (as seen in Figure 1). Figure 4 shows the RBO photometry with the model overlaid. Table 2 contains a list of our priors used as inputs to `exoplanet`.

4.2. Independent RV Validation

To test the validity of our joint fit, we used the simplest case of fitting the RV data with `exoplanet`. We adapted the recipe from Foreman-Mackey et al. (2021a) to fit a single companion using the same RV priors as the joint fit and to create a single Keplerian RV model fixing the eccentricity to zero. Our posterior result for the semiamplitude is 18.26 km s^{-1} with a σ of 0.17 km s^{-1}, which is consistent with our joint fit of the posterior values.

4.3. Joint Fit Using the Secondary Eclipse Model

We built upon our initial joint fit model by adding an additional component to model the secondary eclipse in the TESS data. We adopted part of the recipe from Foreman-Mackey et al. (2021a)[19] by including normal priors of the ratios of the mass (q), radius R_B/R_A, and surface brightness (S). We applied the secondary eclipse function from `exoplanet` to the TESS sectors to model the secondary eclipse. We did not apply the secondary eclipse function to the RBO data as the duration does not include the secondary eclipse portion of the light curve. The secondary eclipse function models the transits using `starry`. As with our initial joint fit, we fixed the eccentricity to zero to improve the stability of the modeling calculation. Solving for eccentricity would be an interesting astrophysical parameter; however, our attempts at allowing this parameter to float caused the model to become unstable. We used two independent quadratic limb-darkening law parameters for the primary star and transiting companion and concluded that our results from this fit are consistent with our single quadratic limb-darkening model.

Figure 5 shows the photometric plot of TESS Sector 20 along with a stellar rotation GP kernel. The detrended photometry is shown in the bottom panel along with the optimized mapped eclipses overlaid before running the HMC. The optimized parameter estimates are then used as the initial conditions when running the HMC. Figure 6 shows the phase-folded photometry data from TESS Sector 20 with the best-fit model posteriors and 1σ interval (16th and 84th percentiles). Figure 7 shows the phase-folded photometric data of the secondary eclipse from TESS Sector 20 with the best-fit model and 1σ interval. Our analysis yields for the companion a mass of $0.080 \pm 0.002 M_\odot$ and a radius of $0.1114^{+0.0048}_{-0.0050} R_\odot$, making the companion, not a planet, but rather a very low mass star, which we designate as TOI-5375 B. Table 4 shows these and other parameters derived from our joint fit analysis.

5. Discussion

Understanding the characteristics of companion objects requires knowledge of the host star. The contrast ratio of exoplanet systems makes secondary eclipse detection nearly impossible. Therefore, deriving the physical parameters for exoplanets is often reliant on the accuracy of stellar evolution models. Eclipsing binary systems, where the secondary's light can be detected, are important for constraining those stellar evolution models. In particular, objects near the hydrogen-burning mass limit, like TOI-5375 B, are able to measure the mass and radius mostly independent of models. An estimate of the companion age would indeed make this a benchmark VLMS.

The simplest way to determine the age of the companion is to assume it is coeval with the primary star, for which we can constrain the age. Isochrone models and asteroseismology are less reliable for low-mass stars than for solar-type stars for determining ages, so age estimates for our M dwarf primary star are weakly constrained at best. One property of low-mass stars we can exploit is the rotation period. M dwarfs lose angular momentum as they age, which results in their rotation period increasing (Engle & Guinan 2011). Therefore, rotation periods can be used to estimate the ages of M dwarfs (see

[19] https://gallery.exoplanet.codes/tutorials/eb/

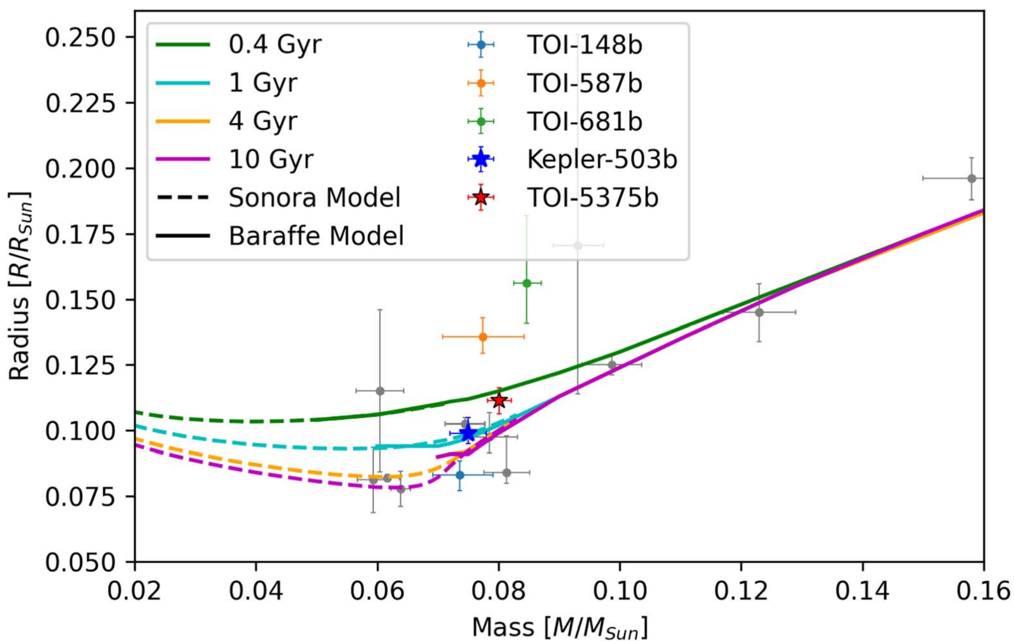

Figure 8. Derived mass and radius of the companion of TOI-5375 plotted with other objects near the hydrogen-burning mass limit. For reference, Kepler-503 is plotted in blue (Cañas et al. 2018); TOI-148, TOI-587, and TOI-681 are plotted in blue, orange, and green, respectively, while other low-mass stars and high-mass substellar companions from von Boetticher et al. (2017) are plotted as gray circles. We show solar metallicity ([M/H] = 0.0) evolutionary isochrone tracks from Baraffe et al. (2015; solid lines) and from (Marley et al. 2021; dashed lines). These models are for substellar companions and low-mass stars and span the ages 0.4, 1, 4, and 10 Gyr.

Barnes 2003; Kiraga & Stepien 2007; Guinan et al. 2016; Popinchalk et al. 2021). Engle & Guinan (2018) provide a relation to calculate the age of an early M dwarf (M0-1 V stars) using its rotational period:

$$t\,(\mathrm{Gyr}) = 0.365 + 0.019 * P_{\mathrm{rot}}^{1.457}(\mathrm{days}). \qquad (1)$$

If we attribute the variability of the host star to evolving starspots over each sector of TESS data, we can use the starspots to extract the rotation period using the period of the GP of $1.9716^{+0.0080}_{-0.0083}$ days. We independently measured the rotation period using the periodogram function from lightkurve (Lightkurve Collaboration et al. 2018) for each TESS sector and a joint periodogram. The joint periodogram yielded a rotation period of ∼1.99 days; this analysis is broadly consistent (2σ) with the rotation period extracted from the GP fit. This period is also visually consistent with the 4% modulation seen in Figure 1. Equation (1) suggests a rotation period derived age of ∼400 Myr. This value is consistent within 1σ of the expected age of an early M dwarf with a rotation period between $1 < P < 10$ days as seen in Newton et al. (2016). However, we note that due to the complex nature of the close binary system, which has potentially significant tidal effects affecting the angular momentum of the system, rotation-based ages derived for single stars and widely separated binaries may not apply.

The depth of the secondary eclipse observed in TESS can be modeled as a function of various fundamental properties (e.g., Charbonneau et al. 2005; Esteves et al. 2013; Shporer 2017):

$$\mathrm{Depth} = \left(\frac{R_2}{R_*}\right)^2 \frac{\int \tau(\lambda) F_{2,\nu}(\lambda, T_2) d\lambda}{\int \tau(\lambda) F_{*,\nu}(\lambda, T_e) d\lambda} + A_g \left(\frac{R_2}{a}\right)^2, \qquad (2)$$

where $\tau(\lambda)$ is the TESS transmission function, T_e and $F_{*,\nu}(\lambda, T_e)$ are the effective temperature and flux of the host star, T_2 and $F_{2,\nu}(\lambda, T_2)$ are the brightness temperature and flux of TOI-5375 B, and A_g is the geometric albedo. For TOI-5375 B, we ignored any contribution to the eclipse depth from reflected light and ellipsoidal variations (e.g., Shporer 2017). We used our posterior distribution to estimate the fluxes of the host star and companion using BT-Settl models (Allard et al. 2012) based on the Caffau et al. (2011) solar abundances. We used `SPISEA` (Hosek & Lu 2020), an open-source python package that simulates simple stellar populations, as an interface to the BT-Settl model grid. This method yields a temperature of 2600 ± 70 K, which is consistent with TOI-5375 B being a late M-type VLMS.

We used the Bayesian Analysis for Nearby Young AssociatioNs Σ (BANYANΣ) to calculate the membership probability of TOI-5375 with any nearby stellar clusters within 150 pc of the Sun (Gagné et al. 2018). BANYANΣ uses multivariate Gaussian models in six-dimensional space on 27 young associations with ages in the range ∼1–800 Myr. Using the coordinates, proper motion, RV, and parallax from the GAIA DR3 archive (Gaia Collaboration et al. 2016, 2022), BANYANΣ indicates a 99.9% likelihood of TOI-5375 being associated with the field.

Figure 8 shows TOI-5375 B plotted on a mass–radius distribution of substellar and other low-mass stars near the hydrogen-burning mass limit. We also show the solar metallicity ([M/H] = 0.0) evolutionary isochrone tracks from Baraffe (Baraffe et al. 2015) and Sonora (Marley et al. 2021). Our mass–radius results are consistent with the 0.4 Gyr model, and this is consistent with our rotation-based estimate of the age of the system. However, in this region of parameter space, isochrones corresponding to older ages begin to fall on top of each other as the stars settle on the main sequence, so at 2σ our radius measurement is consistent with a broad range of isochrone ages. TOI-5375 B is comparable in mass and radius to Kepler-503b (Cañas et al. 2018), although Kepler-503b's age is much older at $\sim$6.7 Gyr. It is gratifying to see that both objects are consistent with the isochrone tracks for their respective ages.

5.1. Additional Observations

Our HPF − SpecMatch analysis measured a spectroscopic $v \sin i_A$ of 16.7 ± 0.9 km s^{-1}. Combining this with the $1.9716^{+0.0080}_{-0.0083}$ day rotation period from our joint fit and stellar radius of $0.632 \pm 0.019 R_\odot$ allows an estimate of the stellar inclination. Using the methodology from Masuda & Winn (2020), and allowing inclination to range from 0° to 180°, yields a stellar inclination estimate of $90° \pm 13°$. Our modeled orbital inclination posterior is $88.41^{+0.97}_{-0.86}$°. Together, our joint fit, the $v \sin i_A$ and rotation period, suggests both the stellar equator and orbit of TOI-5375 B are close to edge-on and most likely well aligned. Independent measurements of the obliquity using the Rossiter–McLaughlin (RM) effect (Triaud 2018) would directly confirm these results. However, due to the relative faintness and length of transit duration (1.74 hr), acquiring RV data from the HET would be nearly impossible, so a different spectrograph, such as MAROON-X (Seifahrt et al. 2022) at Gemini, would be required.

The modulation seen in the different TESS sectors in Figure 1 could be used to deduce the atmospheric circulation (e.g., Bourrier et al. 2020), and future efforts could explore the efficacy of heat circulation in the companion based on the temperature measured in transit and in the eclipse position; however, such an analysis is beyond the scope of this paper.

6. Summary

We present ground-based follow-up data from HPF, NESSI, and RBO and use it along with TESS photometry to carry out an HMC joint fit that characterizes the companion to TOI-5375. This analysis shows TOI-5375 B is a VLMS with a mass of $0.080 \pm 0.002 M_\odot$, a radius of $0.1114^{+0.0048}_{-0.0050} R_\odot$, and a brightness temperature of 2600 ± 70 K on a $1.721553^{+0.000001}_{-0.000001}$ day orbit. The host star has a rotation period of $1.9716^{+0.0080}_{-0.0083}$ days, determined by the spot-induced periodicity in the light curve. The rotation period is suggestive of an age of $\sim$400 Myr measured using single-star evolution of wide binaries and is not associated with any nearby clusters. TOI-5375 is amenable to additional modeling including atmospheric circulation, RM observations to measure obliquity, and the 3D architecture of the orbit.

We acknowledge support from NSF grants AST-1006676, AST-1126413, AST-1310885, AST-1310875, ATI 2009554, ATI 2009889, ATI-2009982, AST-2108512, and the NASA Astrobiology Institute (NNA09DA76A) in the pursuit of precision radial velocities in the NIR. The HPF team also acknowledges support from the Heising-Simons Foundation via grant 2017-0494. C.I.C. acknowledges support by NASA Headquarters through an appointment to the NASA Postdoctoral Program at the Goddard Space Flight Center, administered by USRA through a contract with NASA and the NASA Earth and Space Science Fellowship Program through grant 80NSSC18K1114. G.S. acknowledges support provided by NASA through the NASA Hubble Fellowship grant HST-HF2-51519.001-A awarded by the Space Telescope Science Institute, which is operated by the Association of Universities for Research in Astronomy, Inc., for NASA, under contract NAS5-26555.

Funding for the TESS mission is provided by NASA's Science Mission directorate. The Hobby–Eberly Telescope is a joint project of the University of Texas at Austin, the Pennsylvania State University, Ludwig-Maximilians-Universität München, and Georg-August Universität Gottingen. The HET is named in honor of its principal benefactors, William P. Hobby and Robert E. Eberly. The HET collaboration acknowledges the support and resources from the Texas Advanced Computing Center. We thank the Resident Astronomers and Telescope Operators at the HET for the skillful execution of our observations with HPF. We would like to acknowledge that the HET is built on Indigenous land. Moreover, we would like to acknowledge and pay our respects to the Carrizo & Comecrudo, Coahuiltecan, Caddo, Tonkawa, Comanche, Lipan Apache, Alabama-Coushatta, Kickapoo, Tigua Pueblo, and all the American Indian and Indigenous Peoples and communities who have been or have become a part of these lands and territories in Texas, here on Turtle Island.

Data presented herein were obtained at the WIYN Observatory from telescope time allocated to NN-EXPLORE through the scientific partnership of the National Aeronautics and Space Administration, the National Science Foundation, and the National Optical Astronomy Observatory. WIYN is a joint facility of the University of Wisconsin-Madison, Indiana University, NSF's NOIRLab, the Pennsylvania State University, Purdue University, University of California, Irvine, and the University of Missouri. NESSI was funded by the NASA Exoplanet Exploration Program and the NASA Ames Research Center. NESSI was built at the Ames Research Center by Steve B. Howell, Nic Scott, Elliott P. Horch, and Emmett Quigley. NSF's NOIRLab, managed by the Association of Universities for Research in Astronomy (AURA) under a cooperative agreement with the National Science Foundation. The authors are honored to be permitted to conduct astronomical research on Iolkam Du'ag (Kitt Peak), a mountain with particular significance to the Tohono O'odham. Deepest gratitude to Zade Arnold, Joe Davis, Michelle Edwards, John Ehret, Tina Juan, Brian Pisarek, Aaron Rowe, Fred Wortman, the Eastern Area Incident Management Team, and all of the firefighters and air support crew who fought the recent Contreras fire.

An allocation of computer time from the UA Research Computing High Performance Computing (HPC) at the University of Arizona and the prompt assistance of the associated computer support group is gratefully acknowledged.

The Center for Exoplanets and Habitable Worlds is supported by Penn State and the Eberly College of Science. The Pennsylvania State University campuses are located on the original homelands of the Erie, Haudenosaunee (Seneca, Cayuga, Onondaga, Oneida, Mohawk, and Tuscarora), Lenape (Delaware Nation, Delaware Tribe, Stockbridge-Munsee), Shawnee (Absentee, Eastern, and Oklahoma), Susquehannock, and Wahzhazhe (Osage) Nations. As a land grant institution, we acknowledge and honor the traditional caretakers of these lands and strive to understand and model their responsible stewardship. We also acknowledge the longer history of these lands and our place in that history.

Some of the data presented was obtained from MAST at STScI. Support for MAST for non-HST data is provided by the NASA Office of Space Science via grant NNX09AF08G and by other grants and contracts. This work includes data collected by the TESS mission, which are publicly available from MAST. Funding for the TESS mission is provided by the NASA Science Mission directorate.

This work has made use of data from the European Space Agency (ESA) mission Gaia (https://www.cosmos.esa.int/gaia), processed by the Gaia Data Processing and Analysis Consortium (DPAC, https://www.cosmos.esa.int/web/gaia/dpac/consortium). Funding for the DPAC has been provided by national institutions, in particular the institutions participating in the Gaia Multilateral Agreement.

We thank the anonymous referee for insightful comments that have improved the quality of this work.

Facilities: TESS, RBO, WIYN (NESSI), HET (HPF).

Software: Astropy (Astropy Collaboration et al. 2013, 2018), lightkurve (Lightkurve Collaboration et al. 2018), Matplotlib (Hunter 2007), NumPy (van der Walt et al. 2011), pandas (McKinney 2010), SciPy (Oliphant 2007; Millman & Aivazis 2011).

ORCID iDs

Mika Lambert https://orcid.org/0000-0002-2527-8899
Chad F. Bender https://orcid.org/0000-0003-4384-7220
Shubham Kanodia https://orcid.org/0000-0001-8401-4300
Caleb I. Cañas https://orcid.org/0000-0003-4835-0619
Andrew Monson https://orcid.org/0000-0002-0048-2586
Gudmundur Stefánsson https://orcid.org/0000-0001-7409-5688
William D. Cochran https://orcid.org/0000-0001-9662-3496
Mark E. Everett https://orcid.org/0000-0002-0885-7215
Arvind F. Gupta https://orcid.org/0000-0002-5463-9980
Fred Hearty https://orcid.org/0000-0002-1664-3102
Henry A. Kobulnicky https://orcid.org/0000-0002-4475-4176
Jessica E. Libby-Roberts https://orcid.org/0000-0002-2990-7613
Andrea S. J. Lin https://orcid.org/0000-0002-9082-6337
Suvrath Mahadevan https://orcid.org/0000-0001-9596-7983
Joe P. Ninan https://orcid.org/0000-0001-8720-5612
Brock A. Parker https://orcid.org/0000-0001-9307-8170
Paul Robertson https://orcid.org/0000-0003-0149-9678
Christian Schwab https://orcid.org/0000-0002-4046-987X
Ryan C. Terrien https://orcid.org/0000-0002-4788-8858

References

Agol, E., Luger, R., & Foreman-Mackey, D. 2020, AJ, 159, 123
Allard, F., Homeier, D., & Freytag, B. 2012, RSPTA, 370, 2765
Astropy Collaboration, Price-Whelan, A. M., & Sipőcz, B. M. 2018, AJ, 156, 123
Astropy Collaboration, Robitaille, T. P., & Tollerud, E. J. 2013, A&A, 558, A33
Bailer-Jones, C. A. L., Rybizki, J., Fouesneau, M., Demleitner, M., & Andrae, R. 2021, AJ, 161, 147
Baraffe, I., Homeier, D., Allard, F., & Chabrier, G. 2015, A&A, 577, A42
Barnes, S. A. 2003, ApJ, 586, 464
Bash, F. 2001, in Encyclopedia of Astronomy and Astrophysics, ed. P. Murdin (Boca Raton: CRC Press), 5446
Bessell, M. S. 1990, PASP, 102, 1181
Bourrier, V., Ehrenreich, D., Lendl, M., et al. 2020, A&A, 635, A205
Caffau, E., Ludwig, H. G., Steffen, M., Freytag, B., & Bonifacio, P. 2011, SoPh, 268, 255
Cañas, C. I., Bender, C. F., Mahadevan, S., et al. 2018, ApJL, 861, L4
Cañas, C. I., Kanodia, S., Bender, C. F., et al. 2022, AJ, 164, 50
Cañas, C. I., Stefansson, G., Kanodia, S., et al. 2020, AJ, 160, 147
Charbonneau, D., Allen, L. E., Megeath, S. T., et al. 2005, ApJ, 626, 523
Choi, J., Dotter, A., Conroy, C., et al. 2016, ApJ, 823, 102
Clough, S. A., Shephard, M. W., Mlawer, E. J., et al. 2005, J. Quant. Spec. Radiat. Transf., 91, 233
Collins, K. A., Kielkopf, J. F., Stassun, K. G., & Hessman, F. V. 2017, AJ, 153, 77
Dotter, A. 2016, ApJS, 222, 8
Eastman, J. D., Rodriguez, J. E., Agol, E., et al. 2019, arXiv:1907.09480
Engle, S. G., & Guinan, E. F. 2011, in ASP Conf. Ser. 451, 9th Pacific Rim Conference on Stellar Astrophysics, ed. S. Qain et al. (San Francisco, CA: ASP), 285
Engle, S. G., & Guinan, E. F. 2018, RNAAS, 2, 34
Esteves, L. J., Mooij, E. J. W. D., & Jayawardhana, R. 2013, ApJ, 772, 51
Feinstein, A. D., Montet, B. T., Foreman-Mackey, D., et al. 2019, PASP, 131, 094502
Fitzpatrick, E. L. 1999, PASP, 111, 63
Ford, E. B. 2006, ApJ, 642, 505
Foreman-Mackey, D. 2018, RNAAS, 2, 31
Foreman-Mackey, D., Agol, E., Ambikasaran, S., & Angus, R. 2017, AJ, 154, 220
Foreman-Mackey, D., Luger, R., Agol, E., et al. 2021a, JOSS, 6, 3285
Foreman-Mackey, D., Luger, R., Agol, E., et al. 2021b, exoplanet: Gradient-based probabilistic inference for exoplanet data & other astronomical time series, Zenodo, doi:10.5281/zenodo.5834934
Gaia Collaboration, Prusti, T., & de Bruijne, J. H. J. 2016, A&A, 595, A1
Gaia Collaboration, Vallenari, A., Brown, A. G. A., et al. 2022, arXiv:2208.00211
Gagné, J., Mamajek, E. E., Malo, L., et al. 2018, ApJ, 856, 23
Gan, T., Wang, S. X., Wang, S., et al. 2023, AJ, 165, 17
Green, G. M., Schlafly, E., Zucker, C., Speagle, J. S., & Finkbeiner, D. 2019, ApJ, 887, 93
Guerrero, N. M., Seager, S., Huang, C. X., et al. 2021, ApJS, 254, 39
Guinan, E. F., Engle, S. G., & Durbin, A. 2016, ApJ, 821, 81
Gullikson, K., Dodson-Robinson, S., & Kraus, A. 2014, AJ, 148, 53
Henden, A, Levine, S, Terrell, D, et al. 2018, AAS Meeting Abstracts, 232, 223.06
Hosek, M. W. J., Lu, J. R., Lam, C. Y., et al. 2020, AJ, 160, 143
Howell, S. B., Everett, M. E., Sherry, W., Horch, E., & Ciardi, D. R. 2011, AJ, 142, 19
Hunter, J. D. 2007, CSE, 9, 90
Jenkins, J. M., Twicken, J. D., McCauliff, S., et al. 2016, Proc. SPIE, 9913, 99133E
Kanodia, S., & Wright, J. 2018, RNAAS, 2, 4
Kasper, D. H., Ellis, T. G., Yeigh, R. R., et al. 2016, PASP, 128, 105005
Kesseli, A. Y., Kirkpatrick, J. D., Fajardo-Acosta, S. B., et al. 2019, AJ, 157, 63
Kipping, D. M. 2013, MNRAS, 435, 2152
Kiraga, M., & Stepien, K. 2007, ACTAA, 57, 149-172
Lightkurve Collaboration, Cardoso, J. V. d. M., & Hedges, C. 2018, Lightkurve: Kepler and TESS time series analysis in Python, Astrophysics Source Code Library, ascl:1812.013
Luger, R., Agol, E., Foreman-Mackey, D., et al. 2019, AJ, 157, 64
Mahadevan, S., Ramsey, L. W., Terrien, R., et al. 2014, Proc. SPIE, 9147, 91471G
Marley, M., Saumon, D., Morley, C., et al. 2021, Sonora Bobcat: cloud-free, substellar atmosphere models, spectra, photometry, evolution, and chemistry, Zenodo, doi:10.5281/zenodo.5063476
Masuda, K., & Winn, J. N. 2020, AJ, 159, 81
McKinney, W. 2010, in Proc. the 9th Python in Science Conf. (Austin, TX: SciPy), 51
Millman, K. J., & Aivazis, M. 2011, CSE, 13, 9
Newton, E. R., Irwin, J., Charbonneau, D., et al. 2016, ApJ, 821, 93
Ninan, J. P., Bender, C. F., Mahadevan, S., et al. 2018, Proc. SPIE, 10709, 107092U
Oliphant, T. E. 2007, CSE, 9, 10
Popinchalk, M., Faherty, J. K., Kiman, R., et al. 2021, ApJ, 916, 77
Ramsey, L. W., Adams, M. T., Barnes, T. G., et al. 1998, Proc. SPIE, 3352, 34
Ricker, G. R., Winn, J. N., Vanderspek, R., et al. 2015, JATIS, 1, 014003

Salvatier, J., Wiecki, T. V., & Fonnesbeck, C. 2016, PeerJ Comp. Sci., 2, e55
Scott, N. J., Howell, S. B., Horch, E. P., & Everett, M. E. 2018, PASP, 130, 054502
Seifahrt, A., Bean, J. L., Kasper, D., et al. 2022, Proc. SPIE, 12184, 121841G
Serenelli, A., Weiss, A., Aerts, C., et al. 2021, A&ARv, 29, 4
Shporer, A. 2017, PASP, 129, 072001
Stefansson, G., Cañas, C., Wisniewski, J., et al. 2020, AJ, 159, 100
Torres, G., Andersen, J., & Giménez, A. 2009, A&ARv, 18, 67
Triaud, A. H. M. J. 2018, The Rossiter–McLaughlin Effect in Exoplanet Research (Cham: Springer), 375
van der Walt, S., Colbert, S. C., & Varoquaux, G. 2011, CSE, 13, 22
von Boetticher, A., Triaud, A. H. M. J., Queloz, D., et al. 2017, A&A, 604, L6
Wright, E. L., Eisenhardt, P. R. M., Mainzer, A. K., et al. 2010, AJ, 140, 1868
Yee, S. W., Petigura, E. A., & von Braun, K. 2017, ApJ, 836, 77
Zechmeister, M., Reiners, A., Amado, P. J., et al. 2018, A&A, 609, A12